Probing the analytical cancellation factor relation using Na lidar and nightglow data from the Andes Lidar Observatory

Javier Fuentes[1], Fabio Vargas[2], Pedro Vega[3], Luis Navarro[4], and Gary Swenson[2]

[1]Gemini Observatory Southern Operations Center
[2]University of Illinois at Urbana-Champaign
[3]University of La Serena
[4]Utah State University

November 23, 2022

Abstract

The cancellation factor (CF) is a model for the ratio between gravity wave perturbations in the airglow intensity to those in the ambient temperature and is necessary to estimate the momentum and energy flux and flux divergence of gravity waves in the airglow emissions. This study tests the CF model using T/W Na Lidar data and zenith nightglow observations of the OH and O(1S) emissions. The dataset analyzed was obtained during the campaigns carried out in 2015, 2016, and 2017 at the Andes Lidar Observatory (ALO) in Chile. We have used an empirical method to fit the analytical function that describes the CF for vertically propagating waves and compared the quantities through the ratio of airglow wave amplitude registered as a dominant event in the images to the wave amplitude in the lidar temperature. We show that the analytical relationship underestimates the observational results. We obtained good agreement with respect to the theoretical value for the O(1S) emission line. In contrast, the observational CF ratio deviates by a factor of ~2 from the analytical value for the OH emission.

Probing the analytical cancellation factor relation using Na lidar and night airglow data from the Andes Lidar Observatory

Javier Fuentes[1], Fabio Vargas[2,‡], Pedro Vega[3], Luis Navarro[4], and Gary Swenson[2]

[1] Gemini Observatory Southern Operations Center, Av. Juan Cisternas 1500, c/o AURA casilla 603, La Serena, Chile; jfuentes@gemini.edu

[2] Department of Electrical and Computer Engineering, Remote Sensing & Space Science Laboratory, University of Illinois at Urbana-Champaign, Urbana, Illinois, USA; fvargas@illinois.edu

[3] Faculty of Science, Physics Department, University of La Serena, Av. Juan Cisternas 1200, La Serena, Chile; pvega@userena.cl

[4] Department of Physics, Utah State University, Utah, USA; luis.navarro.dominguez@gmail.com

‡ These authors contributed equally to this work.

1　**Abstract:** The cancellation factor (CF) is a model for the ratio between gravity wave perturbations in
2　the airglow intensity to those in the ambient temperature, and is necessary to estimate the momentum
3　and energy flux and flux divergence of gravity waves in the airglow emissions. This study tests
4　the CF model using T/W Na Lidar data and zenith nightglow observations of the OH and $O(^1S)$
5　emissions. The dataset analyzed was obtained during the campaigns carried out in 2015, 2016,
6　and 2017 at the Andes Lidar Observatory (ALO) in Chile. We have used an empirical method to
7　fit the analytical function that describes the CF for vertically propagating waves, and compared
8　the quantities through the ratio of airglow wave amplitude registered as dominant event in the
9　images to the the wave amplitude in the lidar temperature. We show that the analytical relationship
10　underestimates the observational results. We obtained a good agreement respect to the theoretical
11　value for O(^{1}S) emission line. In contrast, the observational CF ratio deviates by a factor of ~ 2 from
12　the analytical value for the OH emission.

13　**Keywords:** Airglow; All-Sky Imagery; Atmospheric Gravity Waves; Cancellation Factor; Lidar;
14　Mesosphere Low-Thermosphere.)

15　## 1. Introduction

Propagating Atmospheric Gravity Waves (AGWs) perturb major and minor species taking part in the chemical reactions of airglow emissions in the mesosphere and low thermosphere (MLT) region (Hecht et al. 1993[], 1994[]; Swenson et al. 1995[]; Smith et al. 2000[]). Airglow emission brightness fluctuations have been simulated by different aeronomers (Swenson and Gardner, 1998[8] ; Swenson and Liu, 1998[9]; Liu and Swenson, 2003[5]; Vargas et al., 2007[10]) assuming one-dimensional models upon certain atmosphere conditions, gravity waves with various intrinsic parameters and damping rates $(\beta)[e.g.,$ 10].

16　　An analytical expression for the cancellation factor (CF) in the OH nightglow was first derived by
17　Swenson and Gardner (1998) for the observed airglow brightness constitutes a height integral of the
18　VER over the vertical extent of the emission layer. Swenson and Gardner, (1998) related this to the
19　temperature perturbation at the altitude of maximum VER through a so-called "CF". This expression
20　was used by Swenson and Liu (1998) to relate the measurements to wave energy and momentum
21　flux. Liu and Swenson (2003) extended the modeling study for $O_2(b, 0-1)$ atmospheric band and

22 OH Meinel emission allowing to investigate the relations between the amplitude and phase of the
23 airglow perturbations induced by gravity waves from simultaneous measurements in both layers.
24 Finally, Vargas et al., (2007) presented a comprehensible one-dimensional model adding the $O(^1S)$
25 emission line to the study of the night airglow emission in response to the AGW perturbations to
26 explore the vertical flux of horizontal momentum and their wave effects on the atmosphere from
27 the three $O(^1S)$, OH, and $O_2(b)$ airglow layers. The latter study drove the motivation to derive the
28 uncertainties in momentum flux and accelerations due to gravity wave parameters estimated from
29 mesospheric nightglow emissions reported in Vargas (2018)[11].

30 We present the first study for testing the analytical relationship of the cancellation factor using
31 Na Lidar data and nightglow all-sky imagery of the OH and $O(^1S)$ emissions during the observing
32 campaigns carried out through 2015, 2016, and 2017 at the Andes Lidar Observatory (ALO) in Chile.
33 We provide the magnitude of CF for multiple waves detected during these campaigns as well as
34 fundamental intrinsic wave parameters, and their uncertainties.

2. Instrumentation and Methodology

36 The Andes Lidar Observatory (ALO) is an facility for middle and upper atmosphere studies
37 located at 30.3S, 70.7W at an altitude of 2530 m near to Cerro Pachón, Chile. Fig. 1 shows the ALO's
38 infrastructure during daytime. This facility is near to the Chilean Andes mountains and also to
39 the major NSF's OIR Lab observatories in Chile, Gemini 8.1-meter and LSST 8.4-meter diameter
40 optical/infrared telescopes.

Figure 1. Panoramic daytime view of the center of operations at the Andes Lidar Observatory managed by the Remote Sensing and Space Laboratory (RSSS) of the University of Illinois at Urbana-Champaign (UIUC), United States of America.

41 The facility is equipped with a Na resonance-fluorescence lidar (nominal power of 1.5 mW)
42 instrument as shown in Fig. 2 for doing remote sensing of the MLT, measuring temperature, wind
43 velocity, and Na density profiles typically at resolution of 1 minute, 500 meters between 80–105 km;
44 ALO also houses an all-sky imager as shown in Fig. 3. The imager records zenith night airglow images
45 of hydroxyl (OH) Meinel bands and atomic oxygen line emissions. The observations using lidar and
46 imagery systems are carried out in low Moon periods throughout the year. The data set analyzed was
47 obtained at the Andes Lidar Observatory (ALO) during campaigns carried out in 2015, 2016, and 2017
48 as listed in Table 1 and table 2.
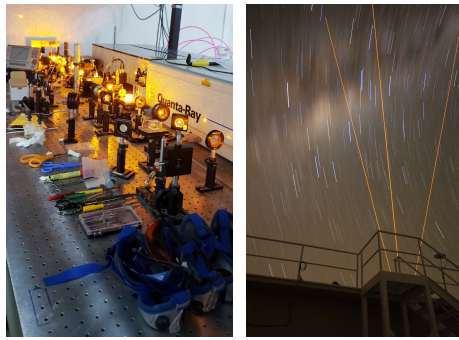
Figure 2. The optical bench of the Na lidar (left) and the Na laser propagated to zenith and off-zenith (right) in the sky. In the long exposed image is captured the star trails and galactic centre.

Figure 3. The All-Sky Imagers: ASI-1 is seen at the left of the picture and ASI-2 at its right side.

Table 1. This table summarizes the observing campaign corresponding to OH and $O(^1S)$ emission lines.

Year	Month	Date	# Nights	# AGWs (OH)	# AGW $O(^1S)$
2015	Jan-Feb	27-30, 02	5	5	5
2015	April	17-25	8	8	3
2015	July	14-25	11	11	11
2015	November	01-08	7	5	2
2016	Feb-Mar	25-29, 01-15	19	14	12
2016	June	06-11	6	6	5
2016	Oct-Nov	23-31, 01-09	17	12	4
2017	April	21-29	8	7	7
2017	November	20-28	9	7	7
2017	December	12-22	10	10	4
	10 campaigns		100	85	60

Table 2. The Lidar data summary is in the following table listed below for each operation period at ALO.

Year, Month, Day	# nights	# Hours	Nights with winds (U^a,V^b)	Average CPS^c
2015 Jan-Feb (16-31, 01-02)	16	96.4	5	559
2015 April (15-29)	14	101.9	8	556
2015 July (14-25)	11	65.3	11	554
2015 November (27-30, 01-08)	8	69.6	7	700
2016 Feb-Mar (25-29, 01-15)	19	96.7	19	540
2016 June (06-11)	6	66.0	6	760
2016 Oct-Nov (23-31, 01-04)	17	91.4	17	582
2017 April (21-29)	8	50.8	8	609
2017 November (20-28)	9	57.0	9	299
2017 December (12-24)	12	70.7	10	213
10 campaigns	155	1043.9	100	7174

^{a}: U represents the zonal winds.
^{b}: V represents the meridional winds.
^{c}: Counts per Shot (CPS), the units of this measurement is photons/cm^2/s/W of the propagating laser power, raw photon count data are processed off-line and preliminary results are shown at the following link: http://lidar.erau.edu/data/nalidar/index.php.

Each individual image represents an uniform 512×512km^2 grid of pixels in geographical coordinates with a resolution of 1 km/pix as shown in Fig. 4. The assumed altitudes for the OH and $O(^1S)$ emissions are 88 km and 95 km, respectively. The integration time for the OH is 60 s and 90 s for the $O(^1S)$. The imager ASI-1 collects the night airglow emissions using the instrumental configuration presented in Table 3:
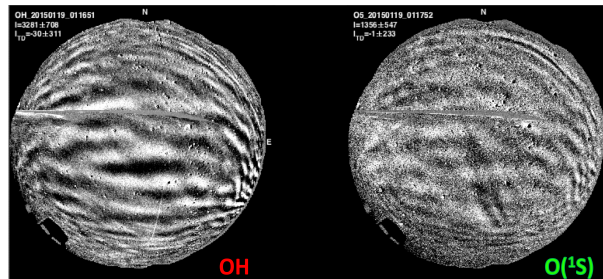
Figure 4. The OH (left) and $O(^1S)$ night airglow emissions is displayed at the right side, both images were captured through the ASI-1 at ALO. The camera field of view is about 1500 km^2.

Table 3. The $O(^1S)$ and $OH(6,2)$ filters were used to estimate the wave amplitude based on the analytical model relating VER measured by the night airglow images to the relative atmospheric density perturbation.

Filter	$\lambda_{center}(nm)$	FWHM (nm)	Exp.time (sec)
$O(^1S)BG$	551.0	3	90
$O(^1S)$	557.7	3	90
$O(^1D)$	630.0	3	75
OH(6-2)	840.0	20	60
$O_2(0-1)$	866.0	7	45

The Na lidar is operated in zenith and off-zenith mode to measure the wind and temperature using the three-frequency technique (She and Yu, (1994)[7]). The laser is locked at the Na resonance frequency at the D2a line, and the two frequencies shifted by ±630 MHz in a sequence. The temperature and line-of-sight wind are derived based on the ratios among the back-scattered signals at these three

⁵⁸ frequencies (Krueger et al., (2015) [4]). Profiles of Na lidar wind and temperature are shown in Fig. 5.
⁵⁹ The integration time in each direction varies between campaigns from 60 to 90 sec, that depends on the
⁶⁰ signal-to-noise ratio retrieved from the photon return.
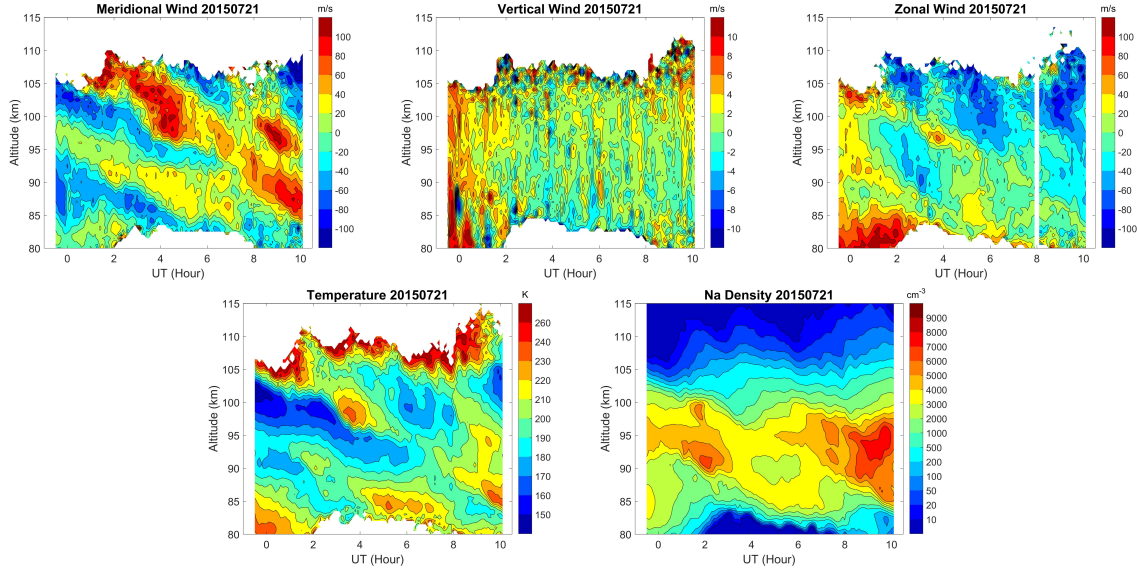
Figure 5. At the top panel is presented the meridional wind (left), vertical wind (middle), and zonal
wind (right) taken on 21 July 2015. Note the nonlinear contour scale (at lowest altitudes) is used to
highlight the low sensitivity of the Na winds in the mesosphere. At the bottom panel is displayed the
temperature (left) and Na density (atoms per cm^3) at the right measured on the same night of 21 July
2015 by the Na lidar at Andes Lidar Observatory in Cerro Pachón, Chile.

⁶¹ The methodology analyzes the perturbations in the airglow intensity in response to gravity waves
⁶² through the wave cancellation effects via CF model. We use the CF empirical model defined as for
⁶³ ratio of the amplitude of I' or T' to the amplitude of the perturbing AGWs at 88 km for OH Meinel
⁶⁴ band emission and 95 km for $O(^1S)$ emission line.
⁶⁵ The observational CF is defined for the airglow intensity as $CF_I = A_I/A_T$. Here, $A_I = I'/\bar{I}$
⁶⁶ and $A_T = T'/\bar{T}$, where primed quantities refer to the wave fluctuation and bar quantities to the
⁶⁷ unperturbed background. A_I is obtained from OH and $O(^1S)$ airglow images processing, and A_T from
⁶⁸ the lidar temperature data at the time of wave perturbation occurrence in the airglow.
⁶⁹ The range of the relative amplitudes in temperature A_T and airglow intensity A_I have been
⁷⁰ chosen to not break the linearity of the solutions. This way, the dispersion and polarization equations
⁷¹ remain valid throughout the analysis. We verify in this way that σ_{λ_z} increases while λ_z decreases. The
⁷² uncertainty in λ_z was derived using equations (8) and (12) reported in Vargas (2018)[11].
⁷³ The night airglow emission in response to AGWs perturbations was modeled using a linear,
⁷⁴ one-dimensional model to describe the temporal and spatial variability of the airglow VER. The
⁷⁵ photochemistry involved in the leading processes to $O(^1S)$ production and the OH Meinel band
⁷⁶ spectrum as well as the intensity and weighted temperature due to upward propagating Atmospheric
⁷⁷ Gravity Waves is described in Vargas et al., (2007)[10].
⁷⁸ There were considered a number of assumptions in the model which include the following: the
⁷⁹ wave amplitudes are small, so that the linear equations can be used to describe AGWs through their
⁸⁰ polarization and dispersion relationships. Also, a wave perturbation of 1% amplitude in temperature
⁸¹ at a reference altitude of $z_r = 85$ km, the background atmosphere specified by the MSIS00 model is
⁸² unchanged by the waves (see Picone et al., (2002)[6]), a windless atmosphere (no shear with altitude),
⁸³ and the waves are propagating vertically through the layers. The simulations consisted in varying the

84 vertical wavelength, λ_z, and the damping coefficient, β, for a single AGW in order to investigate the
85 relationship between wave perturbations, the vertical wavelength, and the VER of the emissions.
86   The intrinsic wave parameters (such as the horizontal wavelength (λ_h), wave orientation (θ),
87 wave phase (ϕ), wave period (τ), horizontal phase velocity (c), and the relative wave amplitude
88 ($I'/\bar{I}$)) have been obtained from the image dataset by performing usual pre-processing routines (i.e.,
89 unwarping, star removal, coordinate transformation, detrending, and filtering) as described in Garcia
90 et al. (1997)[1]). In particular, wave intrinsic periods were inferred mean horizontal winds using from
91 the lidar.
92   In order to compute the temperature perturbations, we removed the mean (T_0) from each
93 temperature altitude to determine $T' = T - T_0$. After selecting short wave periods ($\tau < 1$ hour) from
94 prominent gravity wave events detected in imaging data, we estimate the observational cancellation
95 factor for the two nightglow emissions.
96   We have established the following criteria to filter out undesirable wave parameters obtained
97 from the image processing presented in Table 4. Here, z_r is the altitude in kilometers to obtain the wave
98 amplitude in T for each nightglow layer, which is done by extracting the relative intensity ($I'/\bar{I}$) of the
99 wave, where I' and $\bar{I}$ are the perturbed and non-perturbed airglow intensity. Also, $T'/\bar{T}$ represents the
100 relative wave amplitude in the lidar temperature, and T' is the perturbed temperature and $\bar{T}$ represents
101 the non-perturbed temperature. Thus, the ratio between I and T perturbations is an estimation of the
102 magnitude of CF.

**Table 4.** Criteria used for filtering the data-set for the OH Meinel band and $O(^1S)$ emission line.

Emission	$z_r(km)$	$I'/\bar{I}$	$T'/\bar{T}$	CF intensity	$\lambda_z(km)$	$\tau(min)$
OH	88	≥ 3	$0.75 - 1.25$	≤ 10	$14 - 60$	≥ 12
$O(^1S)$	95	≥ 4	$0.75 - 1.25$	≤ 10	$10 - 60$	≥ 12

103   We have detected prominent AGWs from the image processing in 85 out of 100 nights of the initial
104 sample for the Meinel OH(6,2) band emission. The result of the filtering operation allows for obtaining
105 valid data points for analysis. After filtering the data using the criteria described above, 94 waves
106 events remained on 11 nights in 2015, 113 waves through 19 nights in 2016, and 30 waves on 4 nights in
107 2017 campaigns. There were observed AGWs in 60 nights out of 100 nights for the $O(^1S)$ emission line.
108 After filtering the data, 43 wave events remained along 9 nights in 2015, 50 waves appeared during 9
109 nights in 2016, and 98 AGWs throughout 5 nights in 2017.
110   Finally, We have compared the observational cancellation factor as derived above) against the
111 analytical CF relationship as modeled in Vargas et al. 2007[10], and its uncertainties have been derived
112 by using equation (11) and their fitting coefficients presented in Table 1, and equation (12) (see Vargas
113 (2018)[11]).

3. Results

115   The observational CF is estimated for both OH(6,2) and $O(^1S)$ emission lines during as shown in
116 Figure 6. The measurements of CF values is weakly correlated with the theoretical CF relationship
117 (black continuous line in the graphs) for the OH emission. The agreement is better for $O(^1S)$ in the
118 range of $\lambda_z \sim 20 - 60$ km.
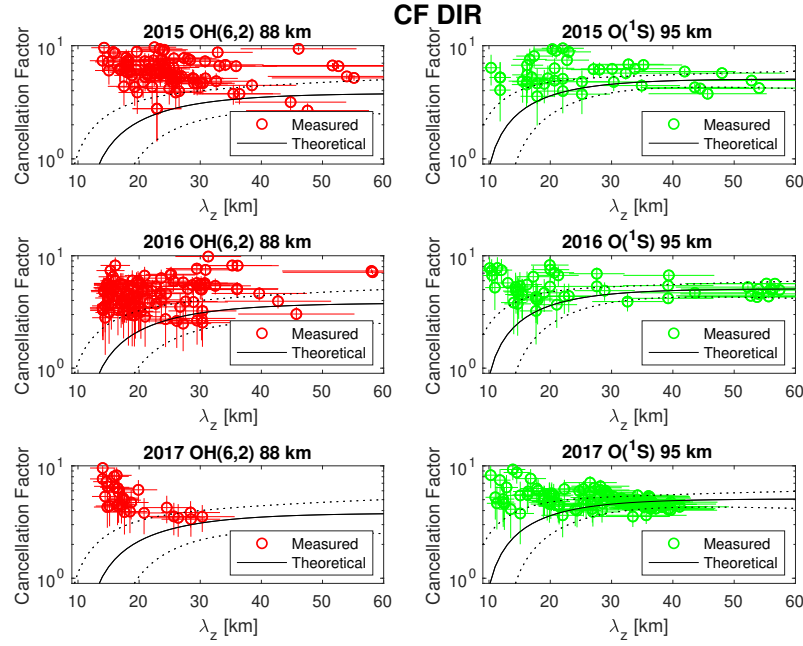
Figure 6. Cancellation factor for OH (red open circles), $O(^1S)$ (green open circles) and their errors. The dashed thin lines denote the 95% confidence bounds (2σ) around the analytic curve shown as the continuous black lines in the plots.

The uncertainties have been derived for λ_z at the OH and $O(^1S)$ emission altitudes. The average value is $\sigma_{\lambda_z} \sim 16\%$ and $\sigma_{\lambda_z} \sim 17\%$ for the OH and $O(^1S)$ emission, respectively. Vargas (2018)[11] found that λ_z shows uncertainties of $\sim 10\%$ and 8% for OH and $O(^1S)$ emissions. The estimated uncertainties in observational CF is $\sigma_{CF} \sim 10\%$ for OH emission and $\sigma_{CF} \sim 7\%$ for the green line $O(^1S)$, respectively. The dashed thin lines in Figure 6 are the 95% confidence levels derived for the analytic CF curve in the model. The uncertainties for both emissions range between 15-24%, and are higher for shorter λ_z. Some observational CF data points fall within the analytic CF confidence levels (black dashed line) for the OH emission (comparable to the full sample), which indicates those points are in agreement with the CF theoretical relationship. Other observational CF are not within the confidence levels of analytic CF, but their uncertainty bars fall within that range, showing consistency between the observed and analytical CFs.
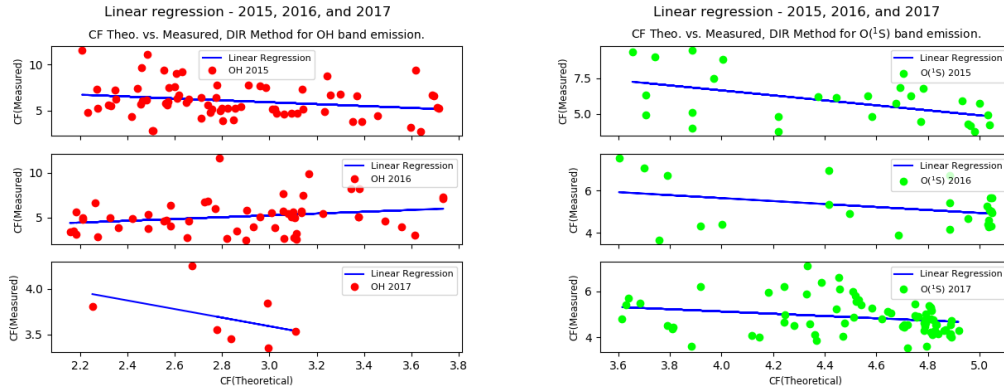

Figure 7. The figure represents the linear regression fit between the observed CF against the analytic CF used to minimize the mean squared error. The R-squared parameter quantifies the percentage of variance our model explains the theoretical relationship for both OH (left) and $O(^1S)$ emissions (right).

130 We have also used a statistical model to examine the correlation between the theoretical and
131 observational CF relationship for $\lambda_z > 20$ km. We have computed the R^2 value of a linear regression
132 fit to the dataset of analytic CF agains observational CF as showed in Fig. 7. Table 5 shows the
133 correlation value of the linear regression in which the CF measured explains the theoretical model
134 for each emission. We see from table 5 that the correlation is higher for the $O(^1S)$ emission than OH
135 emission. Note that there is a few data points for this emission in 2017 that refrain us to make a strong
136 conclusion about its correlation.

Table 5. R-squared values computed from the linear regression model between the CF theoretical and observational for the OH and $O(^1S)$ emission.

Year	R^2(OH)[%]	$R^2(O(^1S))$[%]
2015	23	50
2016	23	35
2017	44	24

137 To estimate how far the data points fall from the CF analytic curve, we have built histograms and
138 kernel density estimators (KDE) using the filtered samples. Figure 8 shows the residuals between the
139 observational and theoretical CF data points. The sample have been filtered out using a 3σ standard
140 deviation to take out all the outliers.
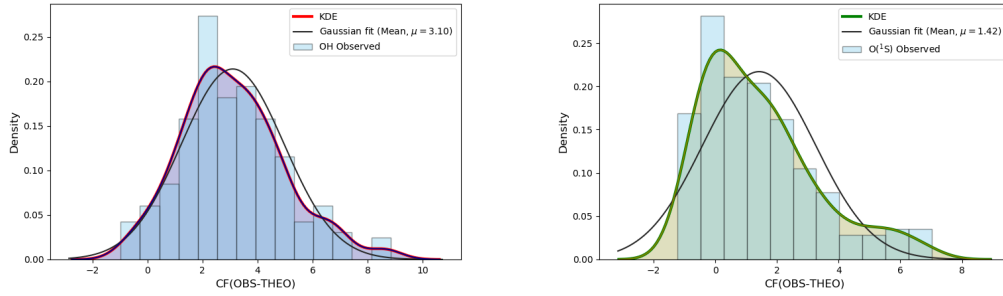
Figure 8. Histograms and density plots of CF_{obs} and CF_{theo} models for the OH and $O(^1S)$ emission.

141 The KDE curve (solid red line) shows the density plot as a smoother version of the histogram.
142 The histogram is normalized by default so that it has the same y-scale as the density plot. Also, we
143 have fitted a Gaussian function with bin width following Freedman-Diaconis rule, which changes the
144 distribution drawn at each data point and the overall distribution. However, we have decided to use
145 the Gaussian kernel density estimation to compute the mean values for both normal distributions.
146 The histograms displayed in Figure 8 have a well defined central tendency in the normal
147 distribution for both OH and $O(^1S)$ emissions. The center of the CF($O(^1S)$) is closer to zero than
148 CF(OH) according to the mean value of the Gaussian curves. The peak of the distribution for both
149 emissions is found to be skewed to the right, meaning that the theoretical model underestimates the
150 observational values. The arithmetic mean values have been derived for the OH and $O(^1S)$ emissions
151 as $\mu_{OH} = 3.1$ and $\mu_{O(^1S)} = 1.42$, respectively.
152 The main contribution of this work is to test the analytical CF relationship using the observational
153 data, and we have verified that the theoretical model underestimate the observations. It is important
154 to measure this discrepancy to make correction to the theoretical relationship for both emissions. To
155 do so, we have evaluated the discrepancy between observed and analytical CF, and add them to the
156 corresponding analytical CF for each layer to obtain corrected predictions.

157   To estimate teh discrepancy, we define the weighted mean and the standard deviation of the mean

158   of the corrected cancellation factor as $\overline{CF} = \frac{\sum_{i=1}^{n} \frac{CF_i}{\sigma^2_{CF_i}}}{\sum_{i=1}^{n} \frac{1}{\sigma^2_{CF_i}}}$ and $\sigma_{\overline{CF}} = \frac{1}{\sqrt{\sum_{i=1}^{n} \frac{1}{\sigma^2_{CF_i}}}}$. We computed the weighted

159   mean and standart deviation as they serve as a measure of the spread in the data. The smaller the

160   spread, the higher accuracy of the measurements. These will have larger influence on the mean and

161   uncertainties, and is a better estimator than the arithmetic mean and standard deviation, which just

162   ignore the magnitude of the error in each measurement. The results are listed in Table 6.

Table 6. The magnitude of the weighted mean and their errors of the direct model for the OH and $O(^1S)$ emission.

Year	CF(OH)	error(OH)	CF($O(^1S)$)	error($O(^1S)$)
2015	5.91	0.26	4.91	0.13
2016	5.48	0.29	4.98	0.07
2017	5.03	0.44	4.76	0.24

163   We summarize next the results from the observational CF weighted mean computation. The

164   weighted mean and weighted errors computed for $O(^1S)$ emission line in 2015, 2016, and 2017 are in

165   good agreement to the theoretical value, $CF_{theo}(O(^1S)) = 5.1$. We did not find a good correlation for

166   the OH emission as the estimated weighted mean is higher than the theoretical CF, $CF_{theo}(OH) = 3.8$.

167   However, our findings help to correct the theoretical CF relationship for the OH emission. Uncertainties

168   derived for CF_{dir} data points have been computed for both emissions. They show that the dispersion

169   of the data set is small compared to its weighted mean. Using the weighted mean values as measure of

170   the discrepancies between CFs, we add them to the analytical curve to adjust its magnitude according

171   to the observation. Figure 9 shows the corrected theoretical CF for both emissions.
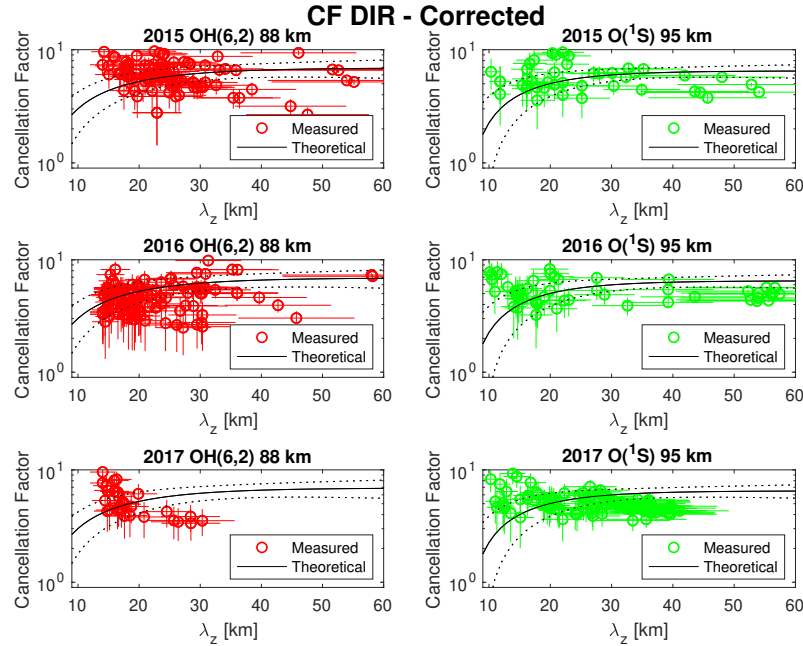
Figure 9. The plots show the observational cancellation factor corrected for both OH (red open circles) and $O(^1S)$ (green open circles) emissions and their errors. The dashed thin lines denotes the 95% confidence bounds around the analytic curve shown as the continuous black lines.

4. Discussion

We have tested the analytic relationship of the cancellation factor (CF) presented in Vargas et al. (2007)[10] for the Meinel OH band emission and $O(^1S)$ emission line using observational data obtained from the Andes Lidar Observatory (ALO).

We report perturbations in the airglow intensity in response to the AGWs through the wave cancellation effect using the empirical method that considers a windless and isothermal atmosphere with upward propagating and saturated waves ($\beta = 1$, the wave amplitude does not change with altitude). Figure 6 shows the cancellation factor in both layers as functions of λ_z. It is clearly seen from the CF definition that smaller CF represents stronger cancellation and that the CF increase asymptotically with increasing λ_z.

The intensity perturbations with small vertical scale ($\lambda_z < 10$ km) have strong cancellation in the layer because of the finite thickness of the airglow layers, which implies that these short λ_z waves do not show significant amplitudes from ground observations (Liu and Swenson (2003)[5]). Thus, the airglow is not sensitive to these waves. Equation (11) in Vargas (2018)[11] shows that the analytic function describing CF increases monotonically with $\lambda_z < 13.86$ km for OH band emission and $\lambda_z < 10.37$ km for $O(^1S)$ emission line, therefore, for λ_z lower than these limits the cancellation effect gets stronger.

The centroid heights and thickness (FWHM) of the unperturbed and standard deviation of the VER profiles derived for the OH layer is larger than that the $O(^1S)$ layer (see Table 1 in Vargas et al. (2007)[10]), which results in a stronger cancellation effect in the OH layer and therefore the CFs for $O(^1S)$ emission is larger than OH, indicating that the greenline airglow is more sensitive to AGWs. This is mainly because the $O(^1S)$ emission is roughly proportional to $[O]^3$ while the OH emission is proportional to [O]. For λ_z larger than ~ 20 km, the layer thickness becomes irrelevant because the layer thickness is a fraction of the vertical wavelength; the layer response is stronger and than virtually the same for longer vertical wavelength waves.

Vargas (2018)[11] presented a comprehensive discussion about the magnitude of the uncertainties in gravity wave parameters estimated from nightglow measurements, and how these uncertainties affect the estimation of key dynamic quantities in the mesosphere and lower thermosphere region. In this study, we have derived the uncertainties in CF and vertical wavelengths which are subject to large uncertainties. However, these magnitudes are in agreement with conclusions reported in [11].

We have found discrepancies between the theoretical model and the observational CF for the OH emission as showed in Table 5. These discrepancies likely come from the photochemical scheme used to model the cancellation factor as it does not use observed atomic oxygen density data (see Vargas et al. (2007)[10]), and the OH photochemical scheme is complex in terms of the chemical reactions. On the other hand, the photochemical scheme for $O(^1S)$ line is simpler and shows better agreement with the observational data.

Also, another discrepancy source is that the model for analytical CF considers only saturated waves only. In a real atmosphere, saturated waves co-exist with dissipative and freely propagating waves. That likely accounts for the majority of the discrepancy in our results because we have not separated waves by their kind in this study, that is, all waves go into our analysis and comparisons with the CF analytic model.

The distribution of atomic oxygen (O) with height in the presence of vertically propagating waves could also influence the result here. These waves are influenced by temperature gradient that affect the rate of chemical reactions of the nightglow emissions (Swenson and Gardner, 1998 [8]). The distribution of species involved in airglow emissions varies considerably with latitude and time, constituting another source of discrepancy between model and measurements (Hickey and Yu (2005)[3]).

Also, based on a full−wave model with the relevant chemistry to the airglow emissions that considers more physical processes such as propagating gravity waves in a non-isothermal mean state, windy (background winds as a function of height $\neq 0$), and viscous atmosphere, the cancellation factor

can vary considerably by a factor of two greater than their isothermal and windless values for gravity waves of short horizontal wavelength with phase velocities less than 100 (m/s), and by a factor of one hundred for phase speeds less than 40 (m/s) (Hickey and Yu (2005)[3]).

Having tested the analytic CF relationship against observational data for two airglow layers, we have found that the theoretical model underestimated the observations for both emissions. The cancellation effect is found to be larger in magnitude for OH band emission than for the $O(^1S)$ emission line. However, CF is valuable to retrieve the magnitude of the relative temperature fluctuation from the airglow, which is used to estimate the momentum flux magnitude transported by the waves (Vargas (2018)[11]).

5. Conclusions

We have used observational data from airglow images and lidar temperature and winds to derive the observational cancellation factor for comparision with the analytical CF model. We quantify the airglow perturbations in the OH and $O(^1S)$ layers generated by gravity waves detected from imagery data taken at ALO from 2015 to 2017. We provide a long-term study in calculating the magnitude of the cancellation factor, fundamental intrinsic wave parameters, and their uncertainties estimated for different solar and seasonal environment scenarios as well as different background conditions provided by the upper atmosphere climatological models (NRLMSISE-00 model) for OH and $O(^1S)$ emission.

A summary of our results is found below:

1. Fig. 6 shows consistency between the analytic and observational CF relationships for the $O(^1S)$ emission in the range $20 < \lambda_z < 60$ km, considering the error bar and 95% confidence levels showed. Using a linear regression model to estimate the correlation between the theoretical and observational CF relationships, we have found a weak correlation for the OH band emission and a larger correlation for the $O(^1S)$ emission line as showed in Table 5.

2. We have found that the analytic relationship underestimates the observational CF. The disagreement showed in Figure 6 were examined through its correlation presented in Table 5 for OH emission. It comes from the fact that dissipative and freely propagating waves co-exist with saturated waves, and we have not separated waves by their kind in this study. That is due to the fact we do not measure individual waves simultaneously in different layers. That would be the only way to assure how the wave amplitude is affect as it moves upwards. Another possible source of inaccuracy could be introduced by the photochemical scheme used to model the cancellation factor. As we explained earlier, the model does not use realistic atomic oxygen data (see Vargas et al., (2007)[10]) to obtain the CF magnitude. As the atomic oxygen density is affected by the season and the solar cycle activity, one way to improve the model and observation agreement is to have the O density calculated for each individual day analyzed. Beyond that, we believe that the distribution of atomic oxygen (O) with height in presence of vertically propagating waves influenced by temperature gradient that affect the rate of chemical reactions of the nightglow emissions (Swenson and Gardner, 1998)[8] would be contributing to the discrepancies as well. By accounting for those effects, it will allow to adjust the coefficients and associated errors of the fitting function for the CF_I for both airglow layers.

3. Because the analytical CF relationship underestimates the observational CF, we have performed a correction in the analytical CF curve by estimating the discrepancies from the data points for both OH and $O(^1S)$ emissions. We used for that the weighted mean and weighted standard deviation to provide a measure of the spread in the data. The adjusted analytical CF shows then a reasonable agreement respect to the observational CF for OH and$O(^1S)$ emissions as in Table 6.

Conflicts of Interest: The authors of this article declare not conflict of interest.

References

1. Garcia, F.J.; Taylor, M.J.; Kelley, M.C. (**1997**), Two-dimensional spectral analysis of mesospheric airglow image data. Appl. Opt. 1997, 36, 7374–7385.

2. Hecht, J. H., R. L. Walterscheid, and M. N. Ross (**1994**), First measurements of the two-dimensional horizontal wave number spectrum from ccd images of the nightglow, Journal of Geophysical Research: Space Physics, 99 (A6), 11,449–11,460, doi:10.1029/94JA00584.

3. Hickey, M. P., and Y. Yu (**2005**), A full-wave investigation of the use of a "cancellation factor" in gravity wave$-$OH airglow interaction studies, J. Geophys. Res., 110, A01301, doi:10.1029/2003JA010372.

4. Krueger, D. A., C.-Y. She, and T. Yuan (**2015**), Retrieving mesopause temperature and line-of-sight wind from full-diurnal-cycle Na lidar observations, Appl. Opt., 54(32), 9469–9489.

5. Liu, A. Z., and G. R. Swenson (**2003**), A modeling study of O_2 and OH airglow perturbations induced by atmospheric gravity waves, J. Geophys. Res., 108(D4), 4151, doi:10.1029/2002JD002474.

6. Picone, J. M., A. E. Hedin, D. P. Drob, and A. C. Aikin (**2002**), NRLMSISE-00 empirical model of the atmosphere: Statistical comparisons and scientific issues, J. Geophys. Res., 107(A12), 1468, doi:10.1029/2002JA009430.

7. She, C. Y., and J. R. Yu (**1994**), Simultaneous three-frequncy Na lidar measurements of radial wind and temperature in the mesopause region, Geophys. Res. Lett., 21(17), 1771–1774.

8. Swenson, G. R., and C. S. Gardner (**1998**), Analytical models for the responses of the mesospheric OH* and Na layers to atmospheric gravity waves, J. Geophys. Res., 103(D3), 6271–6294.

9. Swenson, G. R., and A. Z. Liu (**1998**), A model for calculating acoustic gravity wave energy and momentum flux in the mesosphere from OH airglow, J. Geophys. Res. Lett., 25, 477-480.

10. Vargas, F. A., Swenson, G., Liu, A., and Gobbi, D. (**2007**), O(^{1}S), OH, and O_2(b) airglow layer perturbations due to AGWs and their implied effects on the atmosphere, J. Geophys. Res., 112, D14102, doi:10.1029/2006JD007642.

11. Vargas, Fabio. A. (**2018**), Uncertainties in Momentum Flux and Accelerations due to Gravity wave Parameters Estimated from Mesosphereic Nightglows, doi:10.1016/j.asr.2018.09.039.